



Anode-cathode interchangeable strategy for in situ reviving electrocatalysts' critical active sites for highly stable methanol upgrading and hydrogen evolution reactions

Bin Zhao^a, Chenyu Xu^b, Mohsen Shakouri^c, Renfei Feng^c, Yu Zhang^d, Jianwen Liu^{a,*},
Lei Wang^a, Jiujun Zhang^e, Jing-Li Luo^a, Xian-Zhu Fu^{a,*}

^a Shenzhen Key Laboratory of Polymer Science and Technology, Guangdong Research Center for Interfacial Engineering of Functional Materials, College of Materials Science and Engineering, Shenzhen University, Shenzhen, Guangdong 518055, China

^b Department of Chemical and Materials Engineering, University of Alberta, Edmonton, Alberta T6G 2G6, Canada

^c Canadian Light Source Inc., Saskatoon S7N 0X4, Saskatchewan, Canada

^d Instrumental Analysis Center of Shenzhen University (Lihu Campus), Shenzhen University, Shenzhen, Guangdong 518055, China

^e Institute for Sustainable Energy, College of Sciences, Shanghai University, Shanghai 200444, China

ARTICLE INFO

Keywords:

Nickel sulfide
Anode-cathode exchange
Stable electrocatalysis
Hydrogen generation
Active sites recovery

ABSTRACT

Surface re-construction was a common phenomenon for non-oxide compound electrocatalysts in anodic oxidation reaction in alkaline electrolyte but surface deactivation arising from excessive oxidation/hydroxylation was critical hindrance to the long-term stability. Herein, a unique anode-cathode interchangeable electrocatalysis strategy is proposed for methanol upgrading reaction (MUR) and hydrogen co-generation in membrane-free electrolyzer. A periodical electrolysis is taken place for the Ni₃S₂/CNTs electrode at positive/negative currents over time. Compared with the traditional chronopotentiometry mode, the MUR-HER coupled reactions by periodically switching anode/cathode per hour present an excellent long-term stability at high current densities of $\pm 100 \text{ mA cm}^{-2}$, in which the Faradaic efficiencies for both H₂ and value-added formate are greater than 95%. Substantial experimental results and deep theoretical DFT studies signify that the successful application of this strategy is mainly due to the reversible modulation of oxidation/hydroxylation status on Ni₃S₂ surface, which effectively prevent the surface active structures of electrocatalysts from over-oxidation.

1. Introduction

The green energy fuel of hydrogen with high purity sourced from water electrolysis becomes an ideal countermeasure for the current serious energy and environment circumstances, yet the cathodic hydrogen evolution (HER) is severely restricted by the sluggish anodic half-reaction of oxygen evolution (OER) [1–4]. In very recent years, the selective oxidation of organics (alcohols, aldehydes, amines, etc.), alternative to OER at anode, is highly attractive to less-energy hydrogen generation and acquiring valued-added chemical products simultaneously [2–6]. For instances, methanol is a representative basic liquid organic and its selective oxidation to value-added formate product has been intensively investigated in recent years, which also demonstrates the decrease of energy cost for hydrogen co-generation [6,7]. Nevertheless, it remains grant difficulty to fulfill this unique coupled reaction

with long-term high and steady efficiency. Generally, the two-compartment electrolyzer separated by ion-exchange membrane is employed to avoid the interruption between anode and cathode half-reactions [7–10]. That is, the oxidative products at anode might be reduced again at cathode. Moreover, the severe corrosion of membrane is highly risky at large current density for an application purpose [11]. Hence, organic upgrading reaction integrated with HER in a membrane-free electrolyzer is still challenging, for which many key factors should be taken into consideration together. The development of highly active and selective electrocatalyst is critical for less-energy hydrogen generation and efficient organic upgrading without O₂/CO₂ emission, and the innovative electrocatalytic strategy is also the key to guarantee the long-term stable anodic/cathodic reactions, and critically the value-added chemicals should not be reduced back to the starting organics at cathode.

* Corresponding authors.

E-mail addresses: jwliu@szu.edu.cn (J. Liu), xz.fu@szu.edu.cn (X.-Z. Fu).

<https://doi.org/10.1016/j.apcatb.2022.121082>

Received 15 October 2021; Received in revised form 9 December 2021; Accepted 4 January 2022

Available online 6 January 2022

0926-3373/© 2022 Elsevier B.V. All rights reserved.

On the other hand, nickel chalcogenides are increasingly attractive in electrocatalytic fields, particularly in the promising subjects of organic upgrading-hydrogen evolution co-reactions, since relevant recent works revealed the excellent electrocatalytic activity and reactive selectivity of these nickel sulfides/selenides nanomaterials [6–8,12–17]. In general, the electrocatalytic activity of electrocatalysts are determined by many key factors, such as the dispersibility, conductivity, morphology, porous structures, specific surface area, and the highly important factor of surface chemical states [16–21]. For deeply understanding the electrocatalytic reaction mechanisms, the re-construction of critical active sites on nickel chalcogenide surfaces have been continuously investigated for several years [18–24]. The as-synthesized fresh nickel chalcogenides are commonly considered as pre-catalyst, and the early efforts show that the amorphous oxide layers formed during pre-activation process are critical factors [6,18–20]. Subsequent Raman studies reveal that the electrophilic species of nickel oxyhydroxides (Ni–OOH), in situ formed on the catalyst surface, are assigned as the critical active species for anodic oxidation reaction, particularly effective to react with nucleophilic organic molecules for selective upgrading, accompanied with the $\text{Ni}^{2+}/\text{Ni}^{3+}$ redox cycling [4,6,22–24]. Recent progress exhibits that the unique synergistic effects exist between the critical Ni–OH/Ni–OOH and SO_x/SeO_x species on nickel chalcogenides surface, thus contributing to the high selectivity of alcohols upgrading conversion to value-added carboxylate products [6,7]. Unfortunately, the fine chemical structures (coordination environments, specified bonding parameters, etc.) of these surface active species have not been satisfactorily comprehended yet. The surface oxidation/hydroxylation should inevitably occur during anodic oxidation process in alkaline electrolyte, which had critical influences on the adsorption/desorption performance between catalyst and guest molecules [6,7]. Nevertheless, the non-ignorable deterioration of electrocatalytic activity arising from the excessive oxidation/hydroxylation was the critical hindrance to the long-term stability, which was found as a common phenomenon but unsolved question for many electrocatalysts in electro-oxidation process in alkaline condition [6,25,26]. To this day, it is still challenging to maintain the high activity of these surface active nanostructures for long-term stable electro-oxidative organic upgrading reaction without decay.

In present work, a unique anode-cathode interchangeable electrocatalysis strategy (Scheme 1) is proposed to solve the above problem. The highly dispersed low-dense 3D networks of $\text{Ni}_3\text{S}_2/\text{CNTs}$ nano-heterostructures were used as representative electrocatalysts for methanol upgrading reaction (MUR) and hydrogen co-generation in a membrane-free electrolyzer. Using ISTEP (multi-current steps) mode, a periodical electrolysis is taken place for the working electrode at positive or negative current over time. Compared with the traditional chronopotentiometry (CP) mode, the MUR-HER coupled reactions by periodically switching anode/cathode roles (Scheme 1) per hour present

an excellent stability at high current densities of $\pm 100 \text{ mA cm}^{-2}$, during which H_2 is the only gas product, and formate is the only non-gaseous product soluble in water, in which the faradaic efficiencies of both products are greater than 95%. The substantial experimental results and deep theoretical studies signify that the successful application of this strategy is mainly due to the reversible modulation of oxidation/hydroxylation status on Ni_3S_2 surface. The cyclic recovery of surface active structures can effectively prevent the $\text{Ni}_3\text{S}_2/\text{CNTs}$ electrocatalysts from over-oxidation in order to avoid the performance decay. Therefore, the appropriate oxidation/reduction status of such fine chemical structures could be maintained on Ni_3S_2 surface, thus leading to the long-term stable, highly efficient and selective methanol upgrading reaction and hydrogen co-generation in a membrane-free electrolyzer.

2. Experimental

2.1. Materials and synthesis

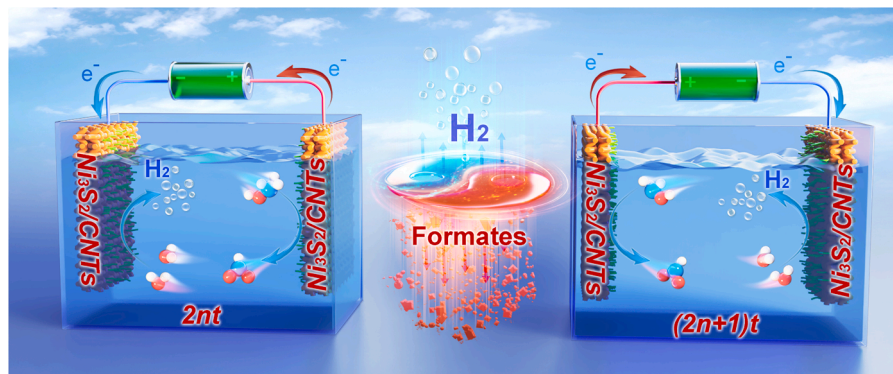
Multi-walled carbon nanotubes, nickel (II) acetylacetonate ($\text{Ni}(\text{acac})_2$), diphenyl disulfide (DPDS), oleylamine (OLA) and Nafion solution were purchased from Sigma-Aldrich. Toluene, methanol, and isopropanol were obtained from Sinopharm Chemical Reagent Co. Ltd. (Shanghai, China). The $\text{Ni}_3\text{S}_2/\text{CNTs}$ nano-heterostructures were synthesized using a modified hot injection method at 220°C , and the detailed synthesis procedure is given in Supplementary data. The stoichiometric molar ratio between $\text{Ni}(\text{acac})_2$ and CNTs has been preliminarily investigated in order to obtain an optimized dispersibility and electrocatalytic activity.

2.2. Catalyst characterization

The chemical, structural and morphological information of as-synthesized $\text{Ni}_3\text{S}_2/\text{CNTs}$ nano-heterostructures were respectively characterized by field emission transmission electron microscopy (FETEM JEM-F200) including selected area electron diffraction (SAED), energy dispersive spectroscopy (EDS) elemental linescan and mapping functions, X-ray powder diffraction (XRD, RIGAKU Smartlab), X-ray photoelectron spectroscopy (XPS, ESCALAB 250Xi), and X-ray absorption fine structure (XAFS) spectra XANES, FT-EXAFS and WT-EXAFS. These characterization methods were described in Supplementary data in detail.

2.3. Electrocatalytic methods

The electrochemical experiments were conducted in a membrane-free electrolyzer. All the electrochemical measurements were conducted in argon saturated electrolyte with the total volume of 500 mL with 1.0 M KOH and 1.0 M methanol in water. The anode-cathode



Scheme 1. Electrocatalysts of $\text{Ni}_3\text{S}_2/\text{CNTs}$ nano-heterostructures employed as electrodes for long-term stable methanol upgrading reaction and efficient hydrogen co-generation in a membrane-free electrolyzer using the anode-cathode interchangeable electrocatalysis strategy.

interchangeable electrocatalysis strategy was performed for methanol upgrading reaction (MUR) and hydrogen co-generation in a membrane-free electrolyzer using Multi-Current Steps (ISTEP) for 20 h. The working electrode was set at periodically interchanged current densities of $+100$ or -100 mA cm^{-2} in 1.0 M KOH solution containing 1.0 M methanol. That is to say, the role of anode or cathode for the same working electrode was exchanged per hour: when the one $\text{Ni}_3\text{S}_2/\text{CNTs}$ electrode was employed as anode for methanol selective oxidation at 100 mA cm^{-2} , the HER was carried out at other $\text{Ni}_3\text{S}_2/\text{CNTs}$ electrode; when the one $\text{Ni}_3\text{S}_2/\text{CNTs}$ electrode played a cathodic role for HER at -100 mA cm^{-2} , the methanol selective oxidation took place at other $\text{Ni}_3\text{S}_2/\text{CNTs}$ electrode as the electron transfer should be balanced in the whole circuit. For comparison, the above MUR-HER coupled reaction was also carried out by chronopotentiometric (CP) at 100 mA cm^{-2} in $1.0 \text{ M KOH} + 1.0 \text{ M}$ methanol solution for 20 h, in which the roles of anodic/cathodic electrodes were not exchanged. Additionally, the preparation of working electrode, type of electrochemical workstation, the electrochemical measurements of linear sweep voltammetry (LSV), and the identification and quantification of H_2 gas and formate products are given in [Supplementary data](#) systematically.

2.4. Structural modeling and theoretical calculation

The lattice parameter of Ni_3S_2 was used for structural modeling, i.e. $a=b=5.731 \text{ \AA}$, $c=7.119 \text{ \AA}$, $\alpha=\beta=90^\circ$, $\gamma=120^\circ$. To model the adsorption of intermediates on the facet $\{110\}$ which was observed experimentally, a $p(3 \times 3)$ supercell ($a=17.357 \text{ \AA}$, $b=12.215 \text{ \AA}$, $c=20.731 \text{ \AA}$, $\alpha=\beta=90.0^\circ$, $\gamma=90.764^\circ$) is made with a vacuum layer of 15 \AA . Vienna ab-initio Simulation Package (VASP) [27,28] was employed for spin-polarized theoretical calculation based on density functional theory (DFT). To account for the strong electron correlation,

the on-site Hubbard corrections ($U_{\text{eff}} = 5.5 \text{ eV}$ for Ni) [29] and dispersion correction [30] were considered in this study. The detailed information of DFT calculation was given in the [Supplementary data](#).

3. Results and discussion

3.1. Structural characterization of electrocatalysts

$\text{Ni}_3\text{S}_2/\text{CNTs}$ heterostructured electrocatalysts were synthesized through a hot injection approach. TEM and XRD are employed for materials characterization. Fig. 1a shows the TEM image of as-prepared $\text{Ni}_3\text{S}_2/\text{CNTs}$, in which Ni_3S_2 nanocrystals are highly dispersed in the low-dense 3D conductive CNTs networks. The magnified TEM image of Fig. 1b presents that the uniform Ni_3S_2 nanocrystals with a small size of $\sim 10 \text{ nm}$ are closely bonded with CNTs to form the hetero-nanostructures. The dispersibility and grain size of Ni_3S_2 nanocrystals are superior to the previous relevant works [7,8,17]. The HRTEM image of Fig. 1c clearly shows an abundant of (110) lattice planes in Ni_3S_2 nanocrystals. These exposed (110) facets on Ni_3S_2 nanostructures have been suggested to exhibit a high selectivity with regard to the methanol selective oxidation to obtain formate [7]. Notably, numerous lattice defects exist in the Ni_3S_2 nanocrystals, and the further magnified HRTEM images of them are given in Fig. S1 ([Supplementary data](#)), indicating that the crystalline lattice fringes are disordered at the edges and interiors of Ni_3S_2 nanocrystals including lattice distortions, dislocations, site defects and amorphous zones. Particularly, they mostly exist at the hetero-interface between Ni_3S_2 nanocrystals and CNTs. Previous studies indicated that the crystal growth of nickel chalcogenide nanoparticles in-situ heterogenized with 1D carbon nanomaterials could induce abundant lattice defects initializing from their hetero-interfaces [6,7]. Fig. S2 ([Supplementary data](#)) shows the charging current

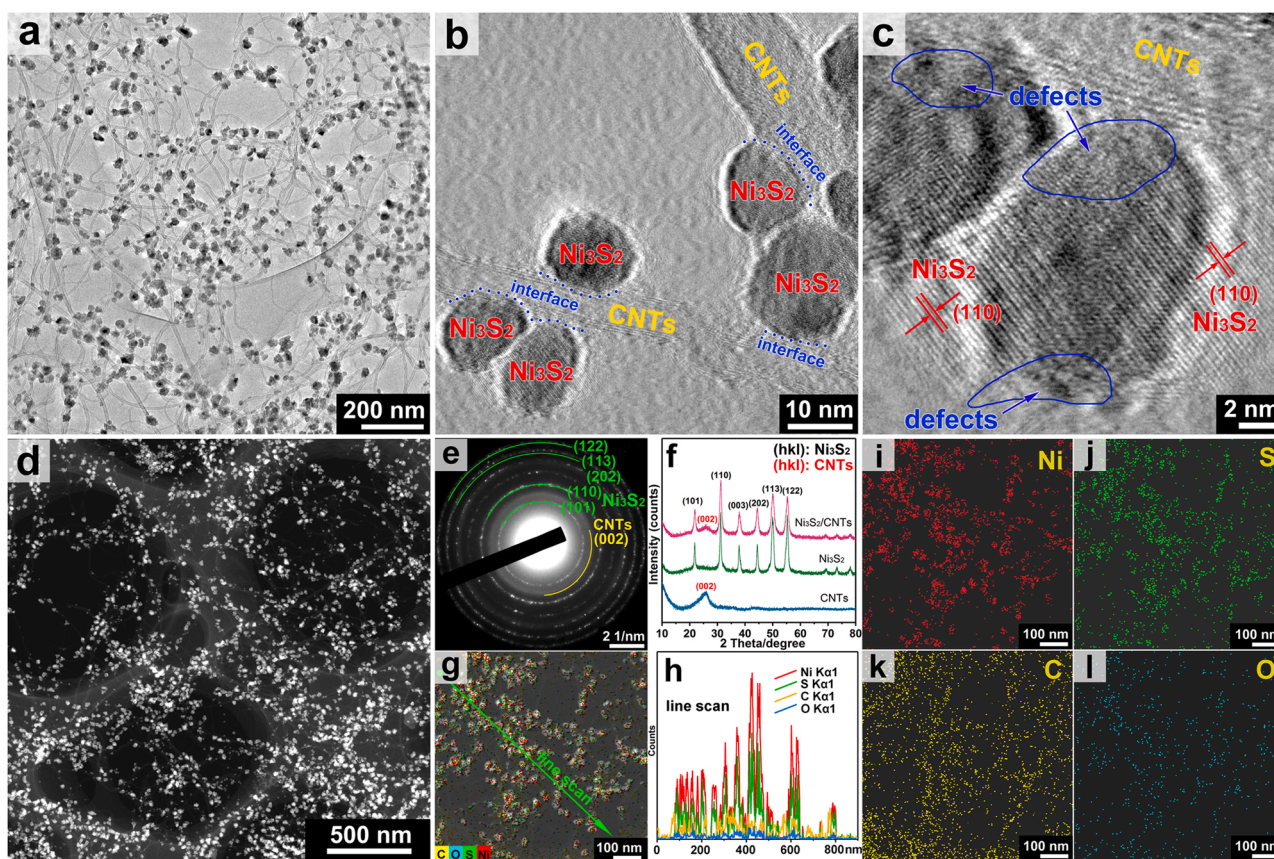


Fig. 1. (a, b) TEM, (c) HRTEM and (d) HAADF-STEM images of highly dispersed Ni_3S_2 nanocrystals heterogenized on CNTs ($\text{Ni}_3\text{S}_2/\text{CNTs}$); (e) SAED pattern; (f) XRD patterns of $\text{Ni}_3\text{S}_2/\text{CNTs}$, pristine Ni_3S_2 nanocrystals, and pristine CNTs; (g-l) EDS elemental line scan and elemental mapping images.

density differences plotted as a function of scan rates in order to evaluate the relative electrochemically active surface areas (ECSA). $\text{Ni}_3\text{S}_2/\text{CNTs}$ nano-heterostructures exhibit much higher relative electrochemically active surface areas than the comparison electrocatalysts of Ni_3S_2 -mixCNTs (Ni_3S_2 physically mixed with CNTs), CNTs and the pristine Ni_3S_2 . Hence, the results confirm that the induced lattice defects would considerably increase the quantity of critical active sites, which are expected to improve the electrocatalytic performance [7,31].

In addition, dark field TEM image (Fig. 1d) confirms the excellent dispersibility of Ni_3S_2 nanocrystals in CNTs networks, suggesting that the 3D cross-linked CNTs networks can effectively avoid the severe aggregation of Ni_3S_2 nanocrystals through spatial quarantine during growth, thus resulting in the low-dense 3D network electrocatalysts beneficial for the fast mass and electron diffusion [6,7]. The rhombohedral heazlewoodite of Ni_3S_2 phase is indicated by both SAED (Fig. 1e) and XRD (Fig. 1f) patterns, in which the lattice planes' spacing corresponds well with PDF # 01-071-1682. The EDS line scan in dark field (Fig. 1g and 1h) shows the nanocrystals with correlated strong Ni and S signals with the Ni/S ratio of about 3/2. The line scan results also confirm the small particles size and high dispersibility of Ni_3S_2 nanocrystals. EDS elemental mapping results (Fig. 1i-l) also present the correlation of Ni and S signals localized with the nanocrystals in Fig. 1g. Both line scan and mapping results suggests the Ni_3S_2 nanocrystals highly dispersed in CNTs networks with extremely low oxidation by oxygen. As indicated by the XPS results in the following Fig. 3c, these very weak O signals should come from the water and hydroxyl groups adsorbed on the surface of fresh $\text{Ni}_3\text{S}_2/\text{CNTs}$.

3.2. Electrocatalytic analysis

The electrochemical studies are carried out in a single compartment electrolyzer without ion exchange membrane. The carbon cloth electrode, modified by $\text{Ni}_3\text{S}_2/\text{CNTs}$, is used for anode/cathode. Fig. 2a gives the LSV curves of $\text{Ni}_3\text{S}_2/\text{CNTs}$ anode in different electrolytes (KOH, KOH with formate, and KOH with methanol) to investigate the electrocatalytic performance of OER and MUR. In KOH solution for OER, O_2

bubbles released from $\text{Ni}_3\text{S}_2/\text{CNTs}$ anode can be observed when the scanning potential reaches 1.50 V (vs. RHE), and the achievement of 100 mA cm^{-2} requires a high potential of 1.65 V (vs. RHE). In addition, the broad peak located at about 1.40 V (vs. RHE) is suggested as the oxidation peak from Ni^{2+} to Ni^{3+} to form $\text{Ni}-\text{OOH}$ species on Ni_3S_2 surface [22–24], indicating that the in situ formed Ni^{3+} ($\text{Ni}-\text{OOH}$) are critical intermediates in the OER process. When methanol is added in KOH solution, the current densities are considerably intensified compared with OER, in which 100, 200, 300 and 400 mA cm^{-2} can be achieved at the working potentials of 1.36, 1.38, 1.40 and 1.42 V (vs. RHE), respectively. In addition, the gas bubbles are unobservable in the LSV measurement, and the pre-oxidation peak for Ni^{3+} ($\text{Ni}-\text{OOH}$) is covered up, suggesting that the nucleophilic methanol molecules could be rapidly oxidized by electrophilic $\text{Ni}-\text{OOH}$ species to overwhelmingly suppress OER [22,32].

With the presence of formate in KOH solution, observable gas bubbles also appear at about 1.50 V. Similar to OER in KOH solution, the broad pre-oxidation peak is also observed at about 1.40 V (vs. RHE), signifying that the critical intermediates of Ni^{3+} ($\text{Ni}-\text{OOH}$) could not easily over-oxidize formate [6]. Nevertheless, the current density in Fig. 2a has an improvement at the potential between 1.45 and 1.60 V (vs. RHE), probably attributed to the increase of electrolyte ions' concentration by adding extra formate ions in KOH solution [20], and these introduced formate ions could optimize the kinetics in OER process on Ni_3S_2 surface. At a potential higher than 1.65 V (vs. RHE), the electrocatalytic activity shows little improvement whether formate exists or not in KOH solution. A supplementary experiment is conducted and the results in Fig. S3 show that formate maintains its concentration after anodic electrolysis, indicating that oxygen evolution is still the dominant reaction despite of the existence of formate. That is, OER is thermodynamically prior to formate's over-oxidation at $\text{Ni}_3\text{S}_2/\text{CNTs}$ anode. In Fig. 2b of the Nyquist plots sourced from electrochemical impedance spectroscopy (EIS), the charge transfer resistance (R_{ct}) is relevant to the electrocatalytic kinetics [33,34]. The R_{ct} is decreased after adding formate into KOH solution, which suggests that the presence of formate ions could reduce the ionic and charge transport resistances so as to

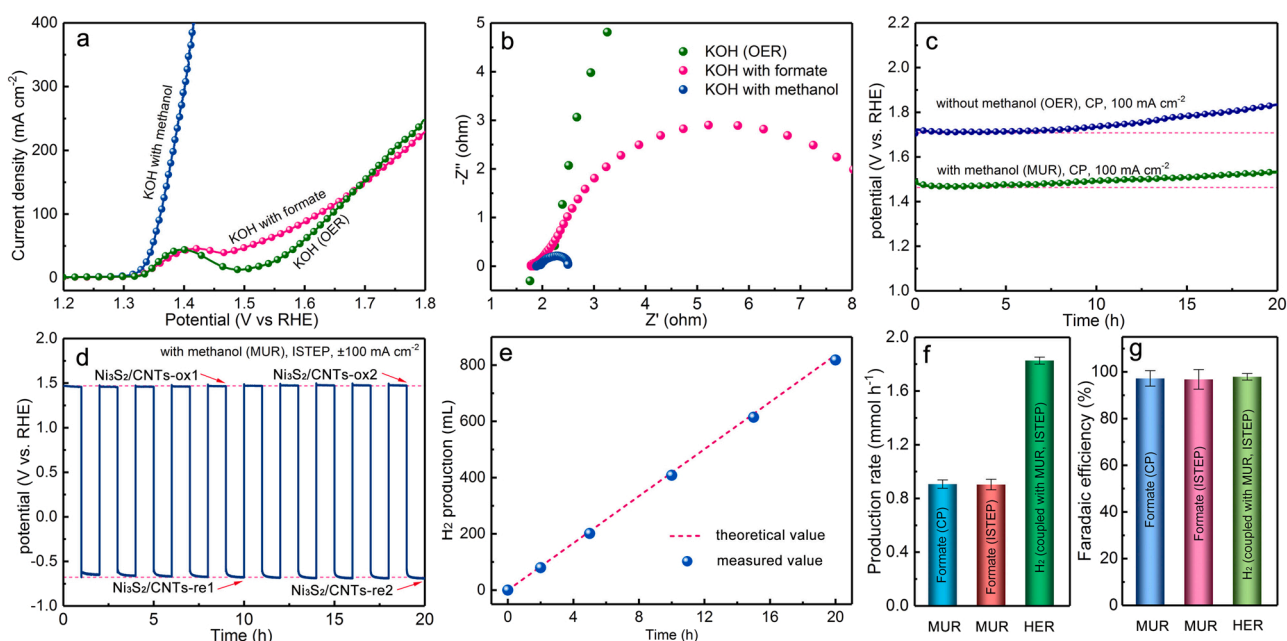


Fig. 2. (a) LSV curves of $\text{Ni}_3\text{S}_2/\text{CNTs}$ anode in different electrolytes (KOH, KOH with formate, and KOH with methanol); (b) Nyquist plots recorded with a frequency range of 0.01–100 kHz; (c) electrocatalytic CP curves for MUR and OER at a fixed current density of 100 mA cm^{-2} for 20 h; (d) the anode-cathode interchangeable electrocatalysis under ISTEP (Multi-Current Steps) at the periodically interchanged current densities of $\pm 100 \text{ mA cm}^{-2}$ for 20 h; (e) the measured H_2 amount from the membrane-free electrolyzer under ISTEP and the calculated theoretical values; (f) the generation rates of formate and H_2 ; (g) the corresponding faradaic efficiencies.

effectively optimize the electrode kinetics for OER. With the addition of methanol, the R_{ct} is considerably decreased to a small value of ~ 0.6 ohm, demonstrating that the electrocatalytic kinetic barrier of methanol oxidation is much lower than that of OER on $Ni_3S_2/CNTs$ anode.

On the other hand, $Ni_3S_2/CNTs$ electrocatalysts are also used as cathode for HER in different electrolytes (KOH, KOH with formate, and KOH with methanol). LSV curves (Fig. S4) show that the addition of formate or methanol in KOH solution has a very slight influence on HER performance, and another supplementary experiment (Fig. S5) confirms that the concentration of formate has little change after 20 h' HER, suggesting that HER is thermodynamically prior to formate's reduction at $Ni_3S_2/CNTs$ cathode.

Fig. 2c shows the CP curves for MUR or OER at a fixed current density of 100 mA cm^{-2} for 20 h. The discussion on the evaluation of energy

cost is given in section 1.7 in the Supplementary data. Previous works also demonstrate that the energy cost is proportionate to the working potential when hydrogen gas is co-generated at the same current density for the same reaction time [6,7]. As shown in Fig. 2c, the working potential of methanol electro-oxidation is ~ 200 mV less than that of OER. Hence, the energy cost of the overall electrolysis can be decreased to boost cathodic H_2 co-generation by intergrating with MUR [6,7]. Nevertheless, the working potential of MUR is slightly increased in the later period of CP curve, and such phenomenon is severe in the OER case. The decay of electrocatalytic activity is probably resulted from the excessive oxidation/hydroxylation on Ni_3S_2 surface [6].

In order to ameliorate the deterioration of catalytic active sites on Ni_3S_2 surface, the anode-cathode interchangeable electrocatalysis is performed under ISTEP. Fig. 2d shows the electrolytic curve with the

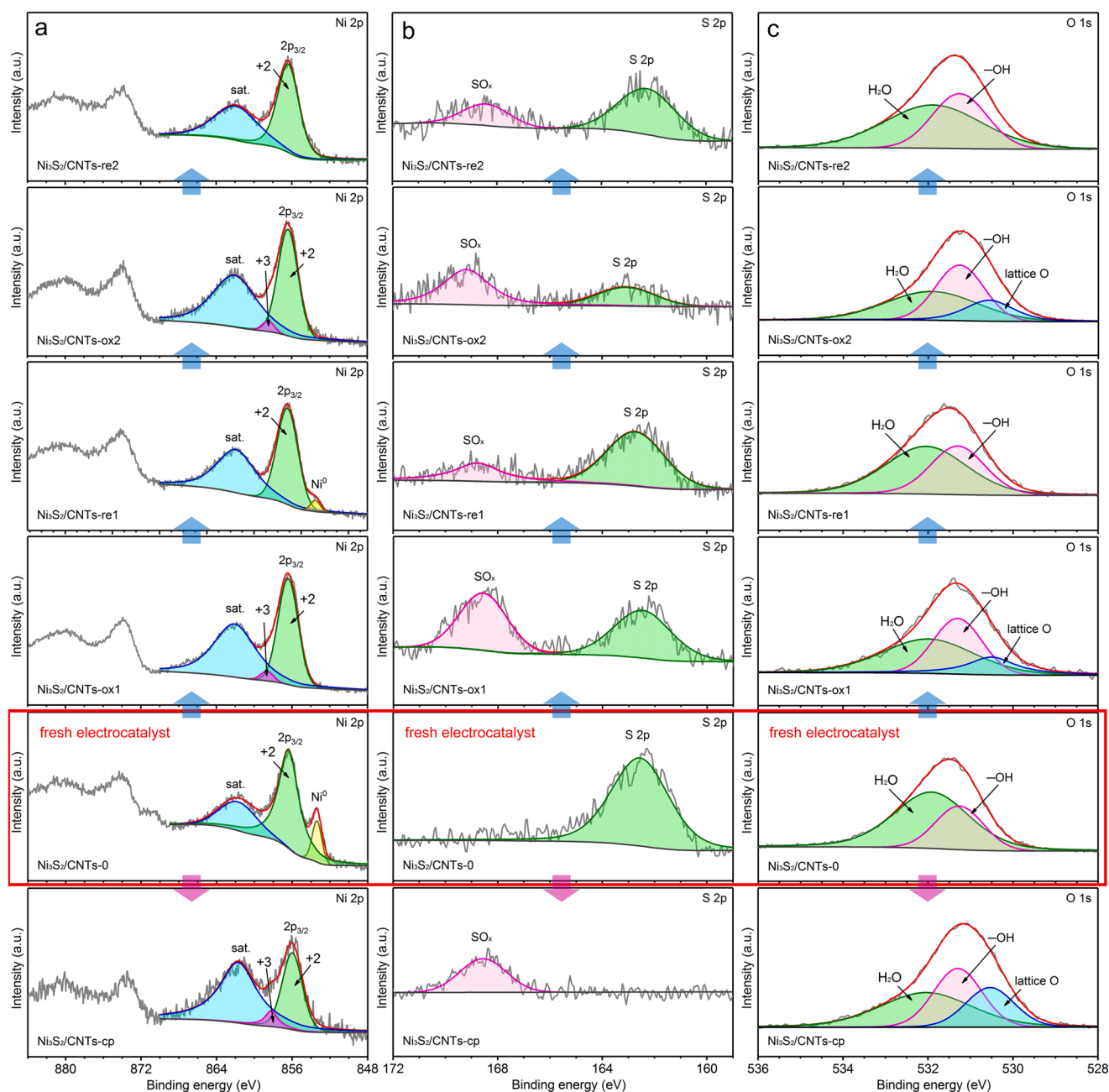


Fig. 3. The comparison of high-resolution (a) Ni 2p, (b) S 2p, and (c) O 1s XPS spectra for fresh electrocatalyst ($Ni_3S_2/CNTs-0$), the used electrocatalyst ($Ni_3S_2/CNTs-cp$) after methanol upgrading reaction under chronopotentiometric (CP) for 20 h, and the used electrocatalyst after 9 ($Ni_3S_2/CNTs-ox1$), 10 ($Ni_3S_2/CNTs-re1$), 19 ($Ni_3S_2/CNTs-ox2$) and 20 ($Ni_3S_2/CNTs-re2$) hours' anode-cathode interchangeable electrocatalysis under ISTEP.

periodically interchanged current densities of $\pm 100 \text{ mA cm}^{-2}$, in which the role of anode/cathode for the same working electrode is exchanged per hour. It demonstrates that the required working potentials increase by $< 1\%$ after 20 h' ISTEP reaction at $|J| = 100 \text{ mA cm}^{-2}$, which indicates the long-term highly stable electrolysis for both anodic oxidation and cathodic reduction through this unique electrolytic strategy. Nevertheless, the electrocatalytic activity of $\text{Ni}_3\text{S}_2/\text{CNTs}$ electrode for MUR shows more obvious decay under CP (Fig. S6, Supplementary data). After 20 h' anode-cathode interchangeable electrocatalysis under ISTEP, the same $\text{Ni}_3\text{S}_2/\text{CNTs}$ electrodes are employed again for the second round of ISTEP reaction for another 20 h. Fig. S7 (Supplementary data) shows the used $\text{Ni}_3\text{S}_2/\text{CNTs}$ can still maintain its high electrocatalytic stability as the required working potential increase by $< 2\%$ after the second round of 20 h' ISTEP reaction. In addition, Fig. 2e indicates that the measured H_2 amount from the membrane-free electrolyzer under ISTEP is in accord with the calculated theoretical values. The formate product obtained from selectively oxidizing methanol is detected by Ion Chromatography (IC) and quantified by the calibration curve of formate in Fig. S8 (Supplementary data). Compared with the electrolytic reaction under CP, the formate product maintains its generation rate under ISTEP (Fig. 2f). The Faradaic efficiencies (Fig. 2g) for both formate and H_2 are greater than 95% under ISTEP, indicating that the $\text{Ni}_3\text{S}_2/\text{CNTs}$ electrode with frequently exchanged anodic/cathodic roles has little adverse effect on the production of value-added formate and H_2 in a membrane-free electrolyzer.

3.3. Systematical investigation of surface active structures

For deeply understanding the efficacious recovery of surface fine nanostructures on $\text{Ni}_3\text{S}_2/\text{CNTs}$ electrocatalysts during ISTEP, the used $\text{Ni}_3\text{S}_2/\text{CNTs}$ electrocatalysts just after 9 ($\text{Ni}_3\text{S}_2/\text{CNTs-ox1}$), 10 ($\text{Ni}_3\text{S}_2/\text{CNTs-re1}$), 19 ($\text{Ni}_3\text{S}_2/\text{CNTs-ox2}$) and 20 ($\text{Ni}_3\text{S}_2/\text{CNTs-re2}$) hours' anode-cathode interchangeable electrolysis under ISTEP (Fig. 2d) were collected for XPS and XAFS analysis. Fig. 3 compares the high-resolution Ni 2p, S 2p, and O 1s XPS spectra between fresh and those used electrocatalysts. The Ni 2p signal (Fig. 3a) of fresh $\text{Ni}_3\text{S}_2/\text{CNTs}$ materials presents a clear peak located at $\sim 853.3 \text{ eV}$ for metallic nickel [22,35], indicating the existence of Ni–Ni interactions on the Ni_3S_2 surface. Moreover, the peak at 856.4 eV corresponds with Ni^{2+} in $2p_{3/2}$ state, accompanied with the satellite peak at $\sim 862.0 \text{ eV}$ [36,37]. A single S 2p peak located at about 162.5 eV (Fig. 3b) indicates the Ni–S interactions with extremely low oxidation of fresh $\text{Ni}_3\text{S}_2/\text{CNTs}$ by oxygen [7,14,15,38], and the O 1s signal (Fig. 3c) shows that the surface of fresh $\text{Ni}_3\text{S}_2/\text{CNTs}$ is mainly covered by water and hydroxyl groups [11,15,16,39]. After a long-term methanol upgrading reaction under CP, the used electrocatalyst ($\text{Ni}_3\text{S}_2/\text{CNTs-cp}$) suffers severe oxidation since the proportion of lattice oxygen increases a lot in O 1s spectrum (Fig. 3c) and the surface sulfur is mainly changed into SO_x species ($\sim 168.6 \text{ eV}$) in S 2p spectrum (Fig. 3b) [5,7,14,15]. Fig. S9 (Supplementary data) presents the XRD pattern of used electrocatalyst ($\text{Ni}_3\text{S}_2/\text{CNTs-cp}$). The peak intensities regarding Ni_3S_2 polymorph are decreased drastically but still distinguishable, compared with the XRD pattern of fresh $\text{Ni}_3\text{S}_2/\text{CNTs}$ in Fig. 1f and using CNTs' diffraction intensity as reference. Meanwhile, new diffraction peaks corresponding to (100) and (110) facets of Ni(OH)₂ (PDF # 00-014-0117) appear in Fig. S9 (Supplementary data) after methanol upgrading reaction under CP, indicating that the surface hydroxylation of Ni_3S_2 is taken place along the preferred orientation of [001] axis of Ni(OH)₂. After 9 h' electrolysis under ISTEP by anode-cathode exchange, Ni^{3+} , SO_x and lattice oxygen signals of $\text{Ni}_3\text{S}_2/\text{CNTs-ox1}$ are detected in Ni 2p, S 2p and O 1s XPS spectra, but these oxidation intensities are much less than those in $\text{Ni}_3\text{S}_2/\text{CNTs-cp}$. $\text{Ni}_3\text{S}_2/\text{CNTs-re1}$ is obtained just after one hour's cathodic reduction reaction from $\text{Ni}_3\text{S}_2/\text{CNTs-ox1}$. XPS results (Fig. 3) indicate that the valence state of nickel is evidently reduced, and the proportions of SO_x and lattice oxygen are considerably decreased. Furthermore, the similar reduction of surface chemical states is also detected by XPS from 19

($\text{Ni}_3\text{S}_2/\text{CNTs-ox2}$) to 20 ($\text{Ni}_3\text{S}_2/\text{CNTs-re2}$) hours' electrolytic reaction under ISTEP, suggesting that the surface chemical states of Ni_3S_2 can be effectively reduced in the cathodic reaction session so as to recover the critical active sites for the next round of anodic reaction.

XAFS measurements are conducted in Total-Electron-Yield (TEY) mode in order to mainly collect the surface fine structural information of $\text{Ni}_3\text{S}_2/\text{CNTs}$ electrocatalysts [40]. The valence states of nickel in fresh and used $\text{Ni}_3\text{S}_2/\text{CNTs}$ electrocatalysts can be examined by the position of absorption edges and the intensity of corresponding white-lines in their normalized XANES spectra in Ni K-edge [7,41,42], as given in Fig. 4a. Compared with the fresh $\text{Ni}_3\text{S}_2/\text{CNTs-0}$, the absorption edge of Ni in $\text{Ni}_3\text{S}_2/\text{CNTs-cp}$ presents an obvious shift to the high energy accompanied with a notable increase of white-line intensity, signifying a severe oxidized state of nickel after the anodic methanol oxidation reaction at a constant current density under CP [6,43]. Interestingly, the position of absorption edge for $\text{Ni}_3\text{S}_2/\text{CNTs-ox2}$ is located between $\text{Ni}_3\text{S}_2/\text{CNTs-0}$ and $\text{Ni}_3\text{S}_2/\text{CNTs-cp}$, and the absorption edge of $\text{Ni}_3\text{S}_2/\text{CNTs-re2}$ shifts further to the low energy accompanied with a decrease of white-line intensity, indicating that an appropriate oxidation situation of Ni_3S_2 surface can be maintained through the anode-cathode interchange electrolysis per hour.

The EXAFS data is analyzed to study the radial distribution function for local atomic structures with regard to the bond length and types [1,6,7,37]. Fig. 4b shows the FT-EXAFS spectra in *R* space for Ni K-edge. The strong and major peak located at around 1.83 Angstrom for the $\text{Ni}_3\text{S}_2/\text{CNTs-0}$ is assigned to the 1st coordination shell of Ni–S scattering interaction, whereas the standard Ni foil presents a typical Ni–Ni scattering path at 2.17 Angstrom [7,42,44]. A contracted averaged scattering radius for Ni atoms' 1st coordination shell demonstrates the intensified oxidation/hydroxylation degree of Ni_3S_2 [7,24], which is denoted as (Ni–S)_{ox} in Fig. 4b. In addition, a severe surface oxidation/hydroxylation is also indicated by the considerably enhanced peak intensity ratio between the 2nd coordination shell for Ni...Ni scattering interaction (majorly Ni–O–Ni) and the 1st coordination shell (Ni–S/Ni–O) [24,37,43].

Compared with the fresh $\text{Ni}_3\text{S}_2/\text{CNTs-0}$, the statistical scattering radius of (Ni–S)_{ox} in $\text{Ni}_3\text{S}_2/\text{CNTs-cp}$ shows an evident contraction to 1.62 Angstrom, accompanied with a drastic peak enhancement of Ni...Ni scattering interaction, indicating that the electrocatalyst suffers from severe surface oxidation/hydroxylation under CP reaction [37]. Nevertheless, the ratios between Ni...Ni and (Ni–S)_{ox} scattering interactions in $\text{Ni}_3\text{S}_2/\text{CNTs-ox2}$ or -re2 are much weaker than that in $\text{Ni}_3\text{S}_2/\text{CNTs-cp}$. The scattering radius of (Ni–S)_{ox} in $\text{Ni}_3\text{S}_2/\text{CNTs-ox2}$ is about 1.68 Angstrom, and such radius expands back to 1.72 Angstrom in $\text{Ni}_3\text{S}_2/\text{CNTs-re2}$ after cathodic reduction reaction for one hour, which result in an optimal dynamic balance to effectively prevent the surface active structures of Ni_3S_2 from over-oxidation.

The wavelet transforms of EXAFS (WT-EXAFS) spectra are demonstrated in Fig. 4c–h, which provide an intuitive display for the 1st and 2nd coordination environments and bonding information of Ni center [6,7,37,45,46]. The first scattering shell's (*R* + α , Angstrom) variation of fresh and used $\text{Ni}_3\text{S}_2/\text{CNTs}$ in WT-EXAFS spectra (Fig. 4d–g) is highly consistent with the FT-EXAFS results (Fig. 4b). Besides, WT-EXAFS spectra can also show the position of WT center (*k*, Angstrom^{−1}), which will generally shift to the lower value if the bonded atoms (with central Ni) supplanted by the lighter element in its coordination shell [31,37,47]. Ni foil (Fig. 4c) presents the sole WT center (*k*) at 7.80 Angstrom^{−1}, which confirms its high metallic nature of Ni–Ni interaction. The WT center (*k*) for fresh $\text{Ni}_3\text{S}_2/\text{CNTs-0}$ (Fig. 4d) is positioned at about 5.34 Angstrom^{−1} for Ni–S scattering interaction, which is decreased to 4.85 Angstrom^{−1} in $\text{Ni}_3\text{S}_2/\text{CNTs-cp}$ (Fig. 4e) after anodic CP reaction, suggesting that a great proportion of Ni–S is displaced by Ni–O bonding [7,31,37]. In addition, a sub WT center with moderate intensity appeared in Fig. 4e, indicated by the red arrow, is expected for the partial formation of Ni–O–Ni 2nd scattering interactions [37,43]. Fig. 4f gives the major WT center of $\text{Ni}_3\text{S}_2/\text{CNTs-ox2}$ (4.99 Angstrom^{−1}),

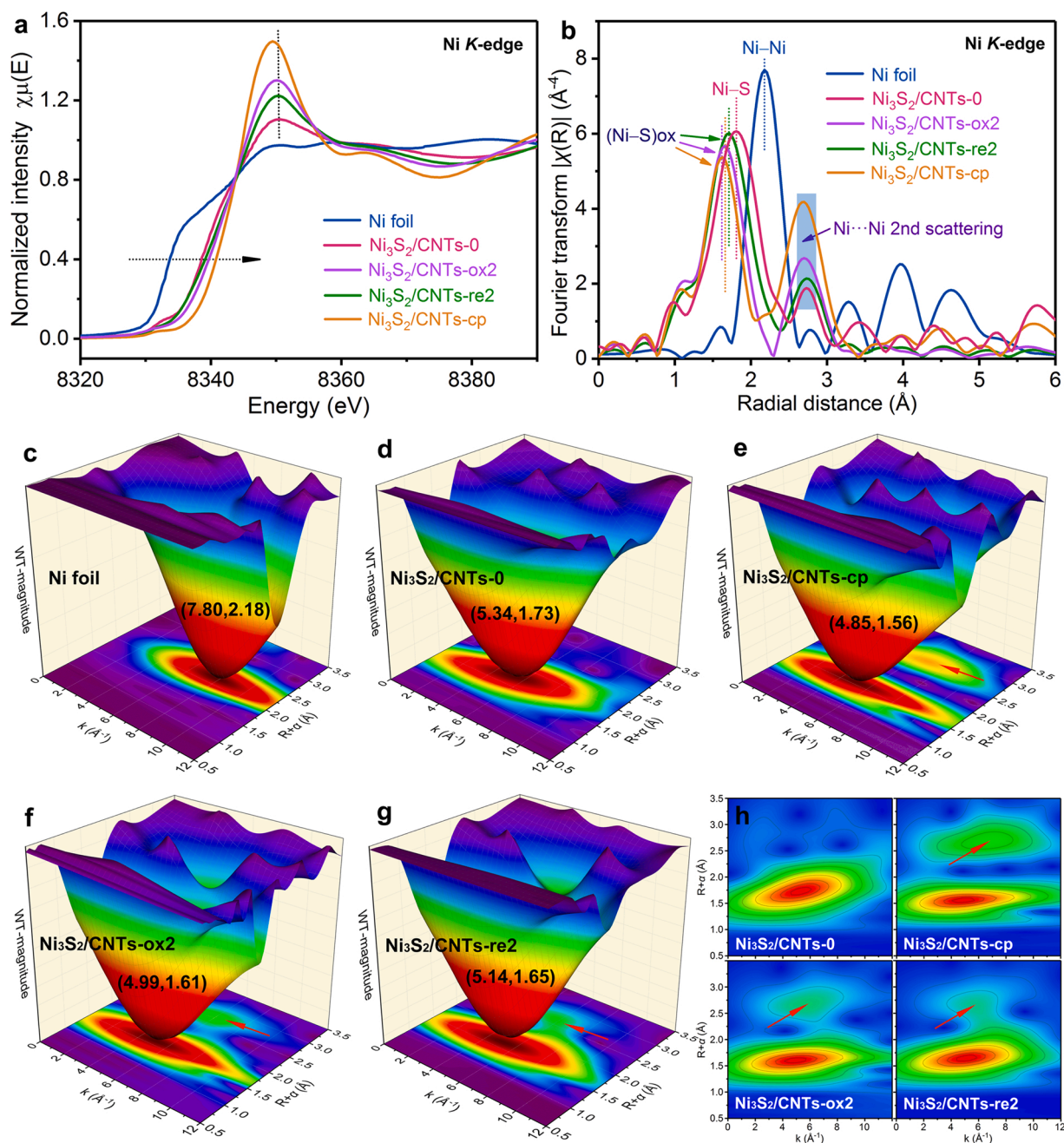


Fig. 4. (a) Normalized Ni K-edge XANES spectra; (b) Fourier transforms of the k^3 -weighted Ni K-edge EXAFS spectra in R space; Wavelet transformed k^2 -weighted EXAFS spectra (WT-EXAFS) for (c) Ni foil, (d) fresh Ni₃S₂/CNTs-0, (e) Ni₃S₂/CNTs-cp, (f) Ni₃S₂/CNTs-ox2 and (g) Ni₃S₂/CNTs-re2; (h) the corresponding 2D graphics of WT-EXAFS spectra.

larger than that of Ni₃S₂/CNTs-cp (4.85 Å⁻¹), which further increases back to 5.14 Å⁻¹ in Ni₃S₂/CNTs-re2 (Fig. 4g) after one hour's cathodic reduction reaction, which is attributed to a decrease of the proportion for Ni-O scattering interaction in Ni₃S₂/CNTs-re2. Meanwhile, the intensity of corresponding sub WT center is also weakened, indicated by red arrow from Figs. 4f to 5g, suggesting a decrease of lattice oxygen in relation to Ni-O-Ni bonding types [37,43]. The discrepancies of sub WT centers between these used Ni₃S₂/CNTs electrocatalysts above are further confirmed in the colorful 2D WT-EXAFS spectra in Fig. 4h and Fig. S10 (Supplementary data). These results indicate that the over-oxidation of Ni₃S₂ surface, majorly in the form of lattice oxygen (e.g. Ni-O-Ni), can be effectively restrained via the unique anode-cathode interchangeable strategy in order to preserve the fine chemical structures of critical active sites on Ni₃S₂ surface by

oxidation/reduction alternation. Taking the electrochemical, XPS and XAFS results into consideration, the anode-cathode interchangeable electrolysis presents an effective strategy to avoid the performance deterioration of Ni₃S₂/CNTs electrocatalysts by periodically recovering the active fine structures on Ni₃S₂ surface, thus keeping the high activity for long-term stable methanol upgrading reaction and H₂ co-generation in a membrane-free electrolyzer.

3.4. DFT studies and mechanistic discussion

Nickel chalcogenides electrocatalysts with typical oxidation/hydroxylation conditions were tentatively investigated in previous works, indicating that surface oxidation/hydroxylation had critical influences on the adsorption/desorption performance between catalyst and guest

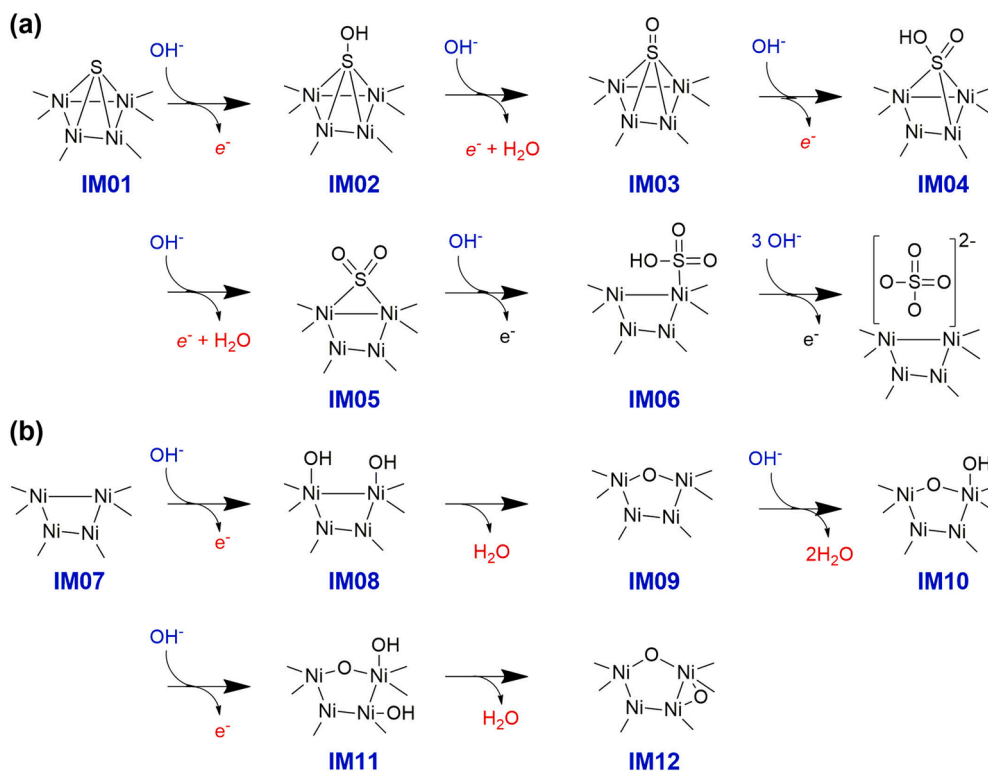


Fig. 5. Illustration of the Ni_3S_2 surface evolution for the oxidation/hydroxylation process when sulfur (a) or nickel (b) atoms exposed on the surface.

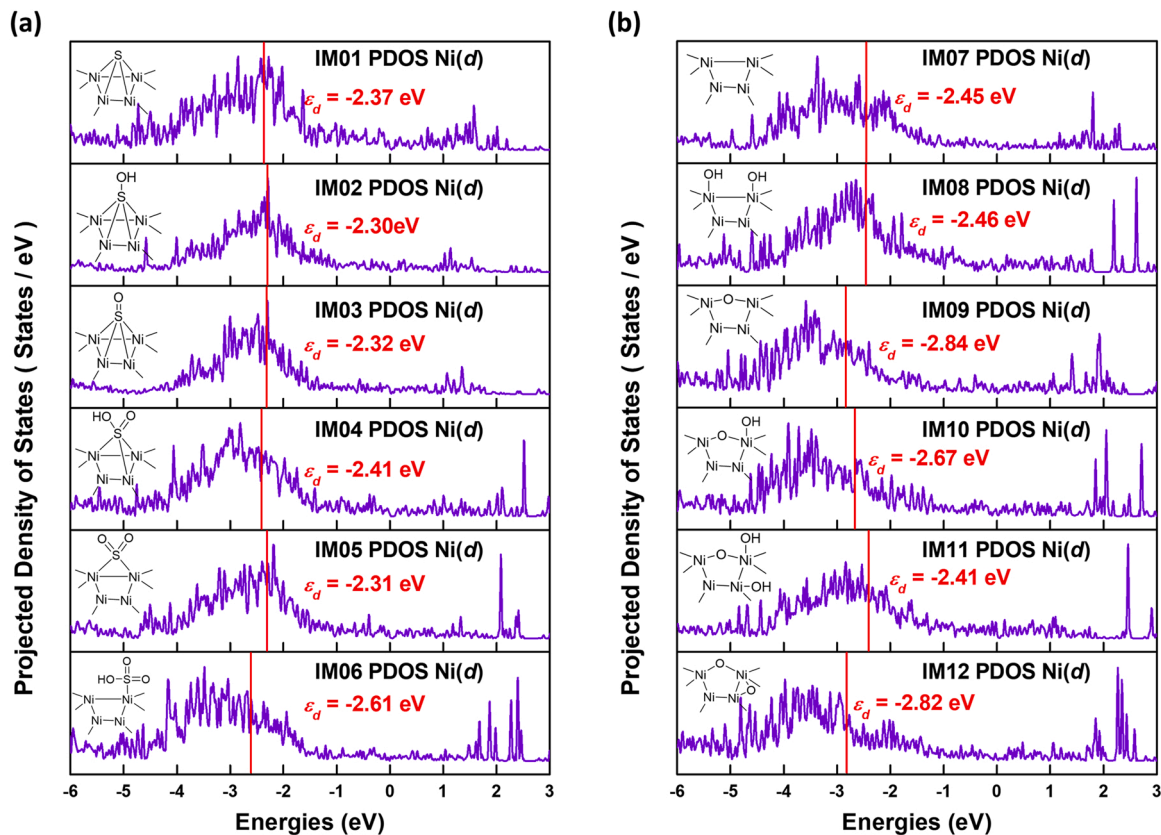


Fig. 6. The 3d orbitals' projected density of states (PDOS) of surface Ni atoms when sulfur (a) or nickel (b) atoms primarily expose on Ni_3S_2 surface with different oxidation/hydroxylation status in line with Fig. 5.

molecules, and the deactivation phenomenon arising from the excessive oxidation/hydroxylation was the critical hindrance to the long-term stability [6,7]. In present work, a strategy of periodical anode/cathode exchange is proposed to solve this problem. The successful application of this strategy is mainly due to the reversible modulation of oxidation/hydroxylation status on Ni_3S_2 surface. As given in Fig. 5, the surface oxidation/hydroxylation fine structures of Ni_3S_2 electrocatalysts is systematically illustrated. The detailed density of states (DOS) analysis resorting to density functional theory (DFT) calculation was performed on the basis of d band theory [48–51].

Both nickel (Ni) and sulfur (S) atoms could be exposed on the surface of Ni_3S_2 when $\text{Ni}_3\text{S}_2/\text{CNTs}$ hetero-nanostructures are used as electrocatalysts. Fig. 5a presents the oxidation/hydroxylation evolution of surface exposed S sites, achieving a series oxidized/ hydroxylated species including S–OH (IM02), S=O (IM03), HO–S=O (IM04), O=S=O (IM05), HSO_3 (IM06), or even resulting in the sulfate that may release from the surface. The projected density of states (PDOS) in Fig. 6a shows the d band center of active Ni sites, namely $\varepsilon_d(\text{Ni})$, which reflect the adsorption properties of the surface. According to the d band theory, the ascending shift of d states approaching Fermi level arising from the reduced filling of anti-bonding states and reinforce of bonding states so as to strengthen the adsorption of guest molecules [48,49]. The $\varepsilon_d(\text{Ni})$ is much close to the Fermi Level in the un-oxidized (–2.37 eV, IM01), slightly hydroxylated (–2.30 eV, IM02) or oxidized (–2.32 eV, IM03) species, suggesting a strong adsorption behavior on these surfaces unfavorable for dissociating the adsorbed reaction intermediates on the basis of Sabatier Principle [50,51]. On the contrary, the over oxidized/hydroxylated of the surface leads to a weaken adsorption (–2.61 eV, IM06). An appropriate oxidization/hydroxylation status with moderate d band center achieves optimal adsorption/desorption activity, which is the best choice for a catalyst. This is the case for IM04 ($\varepsilon_d(\text{Ni})$ = –2.41 eV), which could be the most active site for selective oxidation of methanol.

In addition the exposure of S, the Ni atoms are also possibly exposed on Ni_3S_2 surface for an actual catalyst. Therefore, the oxidation/hydroxylation will also occur on the exposed Ni atoms when electrocatalytic reaction runs in alkaline electrolyte at the anode [11,52]. Fig. 5b shows the oxidation/hydroxylation evolution for the exposed Ni atoms, involving Ni–OH (IM08), Ni–O–Ni (IM09), Ni–OOH (IM10), the unstable surface species of HO–Ni–Ni–OOH (IM11), the formation of lattice oxygen and bridge oxygen bonding (IM12) under over-oxidation. The projected density of states (PDOS) in Fig. 6b shows the $\varepsilon_d(\text{Ni})$ of oxidation/ hydroxylation status IM07–IM12, indicating that un-oxidized Ni and hydroxylated Ni–OH (IM08) possess short distances from their d band center to the Fermi Level, compared with IM09, IM10 and IM12. Consequently, IM07 and IM08 are expected to possess strong adsorption towards guest molecules, which is adverse for the products' desorption in a continuous reaction [50,51]. The surface structure of IM09 with lattice oxygen shows a much negative $\varepsilon_d(\text{Ni})$ = –2.84 eV. In addition, the structure of IM11 is unstable so that the dewatering will quickly take place to form IM12, which possesses both lattice oxygen and bridge oxygen bonding, resulting in the $\varepsilon_d(\text{Ni})$ = –2.82 eV. The surface Ni coordination structures with over-oxidation status (IM09 and IM12) exhibit much negative d band centers that are much far away from Fermi Level, which are expected to have too weak adsorption for the reaction intermediates according to d band theory [48,49]. The surface structure of IM10 with appropriate oxidation/hydroxylation presents a moderate $\varepsilon_d(\text{Ni})$ of –2.67 eV among IM07–IM12, which could make an optimal sorption behavior for reaction intermediates on catalyst surface.

The synergistic effect between SO_x and Ni–OOH has been discussed in our previous work [7]. Taking an actual electrocatalytic reaction into consideration, both Ni and S should exist on Ni_3S_2 surface and both of them should experience the oxidation/hydroxylation status mention above. With the combination of Ni (Figs. 5a, 6a) and S (Figs. 5b, 6b) exposure, it is more reasonable to deduce that the main active center of Ni–OOH (IM10) collaborated with the HO–S=O (IM04) species may

make an optimized adsorption/desorption performance for an optimum activity of electrocatalytic methanol selective upgrading to obtain formate, in accordance with the previous findings and deepening the understanding for the origin at molecular level [7,53].

On the other hand, the reaction mechanism of HER at $\text{Ni}_3\text{S}_2/\text{CNTs}$ cathode is also investigated by DFT calculations. Fig. 7 shows the adsorption energies of critical intermediates for HER on Ni_3S_2 (110) surface, as it is the most commonly exposed surface in Ni_3S_2 nanostructures [7,33] and also demonstrated by HRTEM characterization (Fig. 1c) in this work. It is well known that the alkaline HER contains the following critical stages including the conversion of $^*\text{H}_2\text{O}$, $^*(\text{OH}+\text{H})$ and $^*\text{H}$ intermediates adsorbed on catalyst surfaces (Fig. 7a–d) [1,37,41, 44]. The $\text{Ni}_3\text{S}_2/\text{CNTs}$ electrocatalysts, which have been oxidized/hydroxylated in the previous fragmentation for methanol oxidation reaction at anode, is alternatively playing the cathodic role in HER fragmentation using ISTEP mode. Moreover, XPS and XAFS results indicate that the oxidized/hydroxylated surfaces are effectively reduced during HER when $\text{Ni}_3\text{S}_2/\text{CNTs}$ employed as cathode under reductive environment. Hence, the surface exposed Ni or S sites with reductive states should be the critical active sites for adsorbing $^*\text{H}_2\text{O}$, $^*(\text{OH}+\text{H})$ and $^*\text{H}$ intermediates in HER (Fig. 7a–d). Notably, the dissociation of adsorbed water ($^*\text{H}_2\text{O}$) to form the adsorbed $^*(\text{OH}+\text{H})$ species should be the rate-determining step (Fig. 7b) in the alkaline HER [1,51,54], in which the $^*\text{OH}$ and $^*\text{H}$ initially adsorbed on the site of $^*\text{H}_2\text{O}$ will diffuse on the Ni_3S_2 (110) surface to reach their stable adsorption states respectively.

Besides the mostly reported active center of Ni for HER, the contribution of exposed S sites on Ni_3S_2 (110) surface is also taken into consideration for collaboratively adsorbing the intermediates in this work, which are shown as insets in Fig. 7a–d. DFT results in Fig. 7e indicate that the energy barrier for splitting H_2O to $(\text{OH}+\text{H})$ is 0.93 eV on Ni_3S_2 (110) surface, which is only 0.27 eV higher than the end state of $^*(\text{OH}+\text{H})$ with adsorption energy of –0.58 eV. Such low kinetic energy barrier is expected from the synergistic effect between the Ni and S sites, as illustrated by DFT optimized structure in Fig. 7b. So the subsequent HER process (Fig. 7c–e) can be smoothly taken place on Ni_3S_2 (110) surface in alkaline condition. Taking all the above into consideration, the over-oxidized surface active sites can be efficaciously reduced when the $\text{Ni}_3\text{S}_2/\text{CNTs}$ anode is alternatively used in the cathode fragmentation using ISTEP mode. Attributed by the periodical recovery of surface active sites, a dynamic balance of appropriate oxidation/reduction status of such fine chemical structures could be maintained on Ni_3S_2 surface, thus achieving the high electrocatalytic activity and long-term stable methanol upgrading and hydrogen co-generation.

4. Conclusion

In summary, a unique anode-cathode interchangeable electrocatalysis strategy is proposed in this work for methanol upgrading reaction and hydrogen co-generation in a membrane-free electrolyzer. A periodical electrolysis is taken place for the working electrode at positive/negative current over time using ISTEP mode. Compared with the traditional CP mode, the MUR-HER coupled reactions by periodically switching anode/cathode present an excellent long-term stability at high current densities of $\pm 100 \text{ mA cm}^{-2}$ per hour, during which H_2 is the only gas product, and formate is the only non-gaseous product soluble in water obtained from methanol selective upgrading. The faradaic efficiencies of both products are greater than 95%, indicating the ignorable interruption between anodic MUR and cathodic HER in the membrane-free electrolyzer. According to the d band theory, DFT studies present that the main active center of Ni–OOH collaborated with the HO–S=O species lead to an optimized adsorption/desorption performance for electro-oxidation reaction. Notably, the Ni_3S_2 surface oxidized/hydroxylated in the anodic reaction session could be efficaciously reduced when the same $\text{Ni}_3\text{S}_2/\text{CNTs}$ electrode alternatively plays the cathode role. In addition, DFT results also reveal that the low kinetic energy

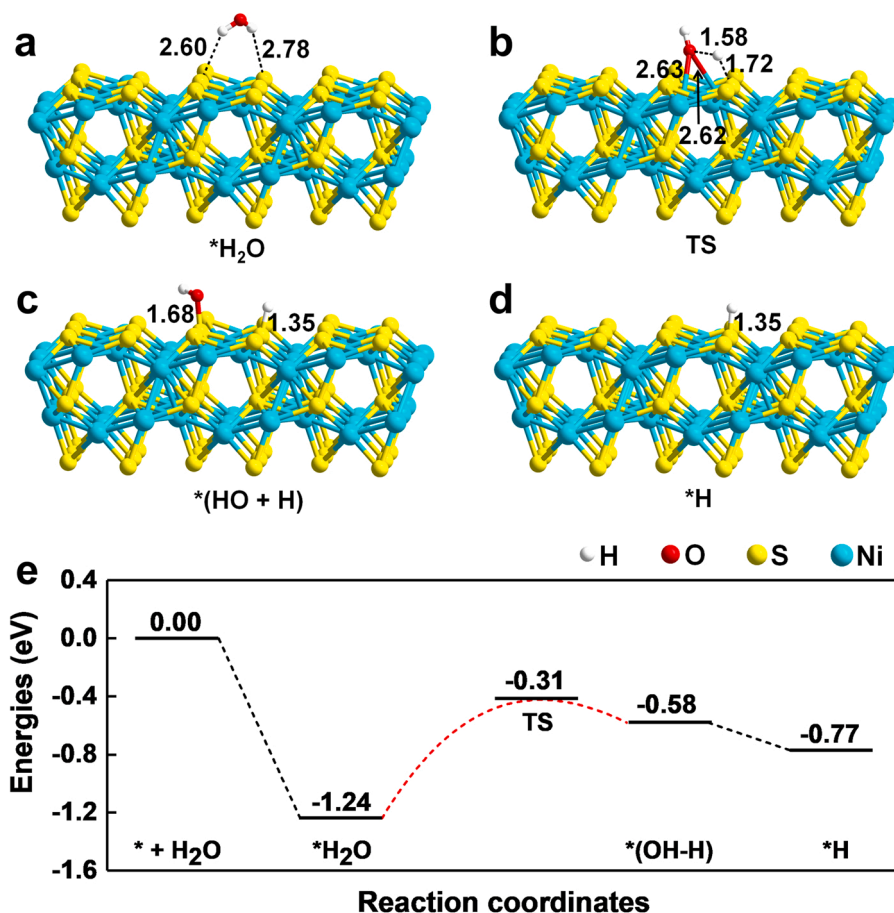


Fig. 7. DFT optimized structures for the intermediates and transition states including the $^*\text{H}_2\text{O}$, $^*(\text{OH}+\text{H})$ and $^*\text{H}$ intermediates and the transition state (TS) from $^*\text{H}_2\text{O}$ to $^*(\text{OH}+\text{H})$ on Ni₃S₂ (110) surfaces (a-d); Gibbs free energy diagrams of HER pathways for the corresponding intermediates and transition states (e).

barrier of the rate-determining step for HER is attributed by the synergistic effect between the Ni and S sites in reductive condition at the cathode. The cyclic recovery of surface active structures can effectively prevent the Ni₃S₂/CNTs electrocatalysts from over-oxidation in order to avoid the performance decay, thus leading to the long-term stable, highly efficient and selective methanol upgrading reaction and hydrogen co-generation in a membrane-free electrolyzer. The unique strategy proposed in this work could considerably stimulate the progress of relevant electrocatalytic fields as an effective and universal countermeasure against the deterioration of electrocatalysts' surface active structures and the performance decay of electro-oxidative anodic reactions.

CRediT authorship contribution statement

Bin Zhao: Conceptualization, Methodology, Validation, Formal analysis, Investigation, Writing - Original Draft, Writing - Review & Editing, Funding acquisition. **Chenyu Xu:** Validation, Software, Formal analysis. **Mohsen Shakouri:** Methodology, Validation. **Renfei Feng:** Methodology, Data Curation, Resources. **Yu Zhang:** Validation, Formal analysis, Resources. **Jianwen Liu:** Conceptualization, Methodology, Software, Formal analysis. **Lei Wang:** Validation, Resources, Visualization, Supervision. **Jiujun Zhang:** Validation, Resources, Supervision. **Jing-Li Luo:** Validation, Resources, Supervision, Project administration, Funding acquisition. **Xian-Zhu Fu:** Conceptualization, Methodology, Validation, Resources, Writing - Review & Editing, Visualization, Supervision, Project administration, Funding acquisition.

Declaration of Competing Interest

The authors declare that they have no known competing financial interests or personal relationships that could have appeared to influence the work reported in this paper.

Acknowledgment

The authors acknowledge the financial support of the National Natural Science Foundation of China (No. 21805187, 21975163) and the Shenzhen Science and Technology Program (No. KQTD20190929173914967, JCYJ20200109110416441). The authors thank Instrumental Analysis Center of Shenzhen University for the assistance with materials characterization and TEM analysis. The authors also thank Shiyanjia Lab (www.shiyanjia.com) for the XPS characterization.

Appendix A. Supporting information

Supplementary data associated with this article can be found in the online version at [doi:10.1016/j.apcatb.2022.121082](https://doi.org/10.1016/j.apcatb.2022.121082).

References

- [1] A. Kumar, V.Q. Bui, J. Lee, A.R. Jadhav, Y. Hwang, M.G. Kim, Y. Kawazoe, H. Lee, Modulating interfacial charge density of NiP₂-FeP₂ via coupling with metallic Cu for accelerating alkaline hydrogen evolution, *ACS Energy Lett.* 6 (2021) 354–363, <https://doi.org/10.1021/acsenenergylett.0c02498>.
- [2] Y. Xu, M. Liu, S. Wang, K. Ren, M. Wang, Z. Wang, X. Li, L. Wang, H. Wang, Integrating electrocatalytic hydrogen generation with selective oxidation of glycerol to formate over bifunctional nitrogen-doped carbon coated nickel-

- molybdenum-nitrogen nanowire arrays, *Appl. Catal. B* 298 (2021), 120493, <https://doi.org/10.1016/j.apcatb.2021.120493>.
- [3] H. Luo, J. Barrio, N. Sunny, A. Li, L. Steier, N. Shah, I.E.L. Stephens, M.-M. Titirici, Progress and perspectives in photo- and electrochemical-oxidation of biomass for sustainable chemicals and hydrogen production, *Adv. Energy Mater.* 11 (2021), 2101180, <https://doi.org/10.1002/aenm.202101180>.
 - [4] Y. Li, X. Wei, L. Chen, J. Shi, Electrocatalytic hydrogen production trilogy, *Angew. Chem. Int. Ed.* 60 (2021) 19550–19571, <https://doi.org/10.1002/anie.202009854>.
 - [5] H. Zhao, D. Lu, J.R. Wang, W.G. Tu, D. Wu, S.W. Koh, P.Q. Gao, Z.C.J. Xu, S. L. Deng, Y. Zhou, B. You, H. Li, Raw biomass electroreforming coupled to green hydrogen generation, *Nat. Commun.* 12 (2021) 2008, <https://doi.org/10.1038/s41467-021-22250-9>.
 - [6] B. Zhao, J. Liu, C. Xu, R. Feng, P. Sui, L. Wang, J. Zhang, J.-L. Luo, X.-Z. Fu, Hollow NiSe nanocrystals heterogenized with carbon nanotubes for efficient electrocatalytic methanol upgrading to boost hydrogen co-production, *Adv. Funct. Mater.* 31 (2021), 2008812, <https://doi.org/10.1002/adfm.202008812>.
 - [7] B. Zhao, J. Liu, X. Wang, C. Xu, P. Sui, R. Feng, L. Wang, J. Zhang, J.-L. Luo, X.-Z. Fu, CO₂-emission-free electrocatalytic CH₃OH selective upgrading with high productivity at large current densities for energy saved hydrogen co-generation, *Nano Energy* 80 (2021), 105530, <https://doi.org/10.1016/j.nanoen.2020.105530>.
 - [8] B. You, S. Liu, N. Jiang, Y. Sun, A general strategy for decoupled hydrogen production from water splitting by integrating oxidative biomass valorization, *J. Am. Chem. Soc.* 138 (2016) 13639–13646, <https://doi.org/10.1021/jacs.6b07127>.
 - [9] P.Y. Liu, K. Shi, W.Z. Chen, R. Gao, Z.L. Liu, H.G. Hao, Y.Q. Wang, Enhanced electrocatalytic nitrogen reduction reaction performance by interfacial engineering of MOF-based sulfides FeNi₂S₄/NiS hetero-interface, *Appl. Catal. B* 287 (2021), 119956, <https://doi.org/10.1016/j.apcatb.2021.119956>.
 - [10] L. Dai, Q. Qin, X. Zhao, C. Xu, C. Hu, S. Mo, Y.O. Wang, S. Lin, Z. Tang, N. Zheng, Electrochemical partial reforming of ethanol into ethyl acetate using ultrathin Co₃O₄ nanosheets as a highly selective anode catalyst, *ACS Cent. Sci.* 2 (2016) 538–544, <https://doi.org/10.1021/acscentsci.6b00164>.
 - [11] Y. Li, X. Wei, L. Chen, J. Shi, M. He, Nickel-molybdenum nitride nanoplant electrocatalysts for concurrent electrolytic hydrogen and formate productions, *Nat. Commun.* 10 (2019) 5335, <https://doi.org/10.1038/s41467-019-13375-z>.
 - [12] Y. Huang, L.-W. Jiang, X.-L. Liu, T. Tan, H. Liu, J.-J. Wang, Precisely engineering the electronic structure of active sites boosts the activity of iron-nickel selenide on nickel foam for highly efficient and stable overall water splitting, *Appl. Catal. B* 299 (2021), 120678, <https://doi.org/10.1016/j.apcatb.2021.120678>.
 - [13] T. Liu, P. Diao, Z. Lin, H. Wang, Sulfur and selenium doped nickel chalcogenides as efficient and stable electrocatalysts for hydrogen evolution reaction: The importance of the dopant atoms in and beneath the surface, *Nano Energy* 74 (2020), 104787, <https://doi.org/10.1016/j.nanoen.2020.104787>.
 - [14] Z.N. Zahran, E.A. Mohamed, Y. Tsubonouchi, M. Ishizaki, T. Togashi, M. Kurihara, K. Saito, T. Yui, M. Yagi, Electrocatalytic water splitting with unprecedented low overpotentials by nickel sulfide nanowires stuffed into carbon nitride scabbards, *Energy Environ. Sci.* (2021), <https://doi.org/10.1039/d1ee00509j>.
 - [15] B. Fei, Z. Chen, J. Liu, H. Xu, X. Yan, H. Qing, M. Chen, R. Wu, Ultrathinning nickel sulfide with modulated electron density for efficient water splitting, *Adv. Energy Mater.* 10 (2020), 2001963, <https://doi.org/10.1002/aenm.202001963>.
 - [16] L. Gao, Z. Liu, J. Ma, L. Zhong, Z. Song, J. Xu, S. Gan, D. Han, L. Niu, NiSe@NiO_x core-shell nanowires as a non-precious electrocatalyst for upgrading 5-hydroxymethylfurfural into 2,5-furandicarboxylic acid, *Appl. Catal. B* 261 (2020), 118235, <https://doi.org/10.1016/j.apcatb.2019.118235>.
 - [17] S.C. Huang, Y.Y. Meng, Y.F. Cao, F. Yao, Z.J. He, X.X. Wang, H. Pan, M.M. Wu, Amorphous NiWO₄ nanoparticles boosting the alkaline hydrogen evolution performance of Ni₃S₂ electrocatalysts, *Appl. Catal. B* 274 (2020), 119120, <https://doi.org/10.1016/j.apcatb.2020.119120>.
 - [18] K. Xu, H. Ding, H. Lv, S. Tao, P. Chen, X. Wu, W. Chu, C. Wu, Y. Xie, Understanding structure-dependent catalytic performance of nickel selenides for electrochemical water oxidation, *ACS Catal.* 7 (2017) 310–315, <https://doi.org/10.1021/acscatal.6b02884>.
 - [19] B.R. Wygant, K. Kawashima, C.B. Mullins, Catalyst or precatalyst? The effect of oxidation on transition metal carbide, pnictide, and chalcogenide oxygen evolution catalysts, *ACS Energy Lett.* 3 (2018) 2956–2966, <https://doi.org/10.1021/acscenergylett.8b01774>.
 - [20] Y. Shi, W. Du, W. Zhou, C. Wang, S. Lu, S. Lu, B. Zhang, Unveiling the promotion of surface-adsorbed chalcogenate on the electrocatalytic oxygen evolution reaction, *Angew. Chem. Int. Ed.* 59 (2020) 22470–22474, <https://doi.org/10.1002/anie.202011097>.
 - [21] Y. Zhu, H.-C. Chen, C.-S. Hsu, T.-S. Lin, C.-J. Chang, S.-C. Chang, L.-D. Tsai, H. M. Chen, Operando unraveling of the structural and chemical stability of p-substituted CoSe₂ electrocatalysts toward hydrogen and oxygen evolution reactions in alkaline electrolyte, *ACS Energy Lett.* 4 (2019) 987–994, <https://doi.org/10.1021/acscenergylett.9b00382>.
 - [22] Y. Huang, X. Chong, C. Liu, Y. Liang, B. Zhang, Boosting hydrogen production by anodic oxidation of primary amines over a NiSe nanorod electrode, *Angew. Chem. Int. Ed.* 57 (2018) 13163–13166, <https://doi.org/10.1002/anie.201807717>.
 - [23] M.T. Bender, Y.C. Lam, S. Hammes-Schiffer, K.-S. Choi, Unraveling two pathways for electrochemical alcohol and aldehyde oxidation on NiOOH, *J. Am. Chem. Soc.* 142 (2020) 21538–21547, <https://doi.org/10.1021/jacs.0c10924>.
 - [24] W. Chen, C. Xie, Y. Wang, Y. Zou, C.-L. Dong, Y.-C. Huang, Z. Xiao, Z. Wei, S. Du, C. Chen, B. Zhou, J. Ma, S. Wang, Activity origins and design principles of nickel-based catalysts for nucleophilic electrooxidation, *Chem* 6 (2020) 2974–2993, <https://doi.org/10.1016/j.chempr.2020.07.022>.
 - [25] J. Li, C. Xing, Y. Zhang, T. Zhang, M.C. Spadaro, Q. Wu, Y. Yi, S. He, J. Llorca, J. Arbiol, A. Cabot, C. Cui, Nickel iron diselenide for highly efficient and selective electrocatalytic conversion of methanol to formate, *Small* 17 (2021), 2006623, <https://doi.org/10.1002/smll.202006623>.
 - [26] L.F. Gao, Z.B. Liu, J.L. Ma, L.J. Zhong, Z.Q. Song, J.A. Xu, S.Y. Gan, D.X. Han, L. Niu, NiSe@NiO_x core-shell nanowires as a non-precious electrocatalyst for upgrading 5-hydroxymethylfurfural into 2,5-furandicarboxylic acid, *Appl. Catal. B* 261 (2020), 118235, <https://doi.org/10.1016/j.apcatb.2019.118235>.
 - [27] G. Kresse, J. Furthmüller, Efficient iterative schemes for ab initio total-energy calculations using a plane-wave basis set, *Phys. Rev. B* 54 (1996) 11169–11186, <https://doi.org/10.1103/physrevb.54.11169>.
 - [28] G. Kresse, J. Furthmüller, Efficiency of ab-initio total energy calculations for metals and semiconductors using a plane-wave basis set, *Comp. Mater. Sci.* 6 (1996) 15–50, [https://doi.org/10.1016/0927-0256\(96\)00008-0](https://doi.org/10.1016/0927-0256(96)00008-0).
 - [29] J. Zaffran, M.C. Toroker, Benchmarking density functional theory based methods to model NiOOH material properties: Hubbard and van der Waals corrections vs hybrid functionals, *J. Chem. Theory Comput.* 12 (2016) 3807–3812, <https://doi.org/10.1021/acs.jctc.6b00657>.
 - [30] S. Grimme, Semiempirical GGA-type density functional constructed with a long-range dispersion correction, *J. Comput. Chem.* 27 (2006) 1787–1799, <https://doi.org/10.1002/jcc.20495>.
 - [31] X. Zheng, X. Han, Y. Cao, Y. Zhang, D. Nordlund, J. Wang, S. Chou, H. Liu, L. Li, C. Zhong, Y. Deng, W. Hu, Identifying dense NiSe₂/CoSe₂ heterointerfaces coupled with surface high-valence bimetallic sites for synergistically enhanced oxygen electrocatalysis, *Adv. Mater.* 32 (2020), 2000607, <https://doi.org/10.1002/adma.202000607>.
 - [32] H.B. Tao, Y. Xu, X. Huang, J. Chen, L. Pei, J. Zhang, J.G. Chen, B. Liu, A general method to probe oxygen evolution intermediates at operating conditions, *Joule* 3 (2019) 1498–1509, <https://doi.org/10.1016/j.joule.2019.03.012>.
 - [33] L. Li, C. Sun, B. Shang, Q. Li, J. Lei, N. Li, F. Pan, Tailoring the facets of Ni₃S₂ as a bifunctional electrocatalyst for high-performance overall water-splitting, *J. Mater. Chem. A* 7 (2019) 18003–18011, <https://doi.org/10.1039/C9TA05578A>.
 - [34] J. Zheng, X.L. Chen, X. Zhong, S.Q. Li, T.Z. Liu, G.L. Zhuang, X.N. Li, S.W. Deng, D. H. Mei, J.G. Wang, Hierarchical porous NC@CuCo nitride nanosheet networks: highly efficient bifunctional electrocatalyst for overall water splitting and selective electrooxidation of benzyl alcohol, *Adv. Funct. Mater.* 27 (2017), 1704169, <https://doi.org/10.1002/adfm.201704169>.
 - [35] W. Zang, T. Sun, T. Yang, S. Xi, M. Waqar, Z. Kou, Z. Lyu, Y.P. Feng, J. Wang, S. J. Pennycook, Efficient hydrogen evolution of oxidized Ni-N₃ defective sites for alkaline freshwater and seawater electrolysis, *Adv. Mater.* 33 (2021), 2003846, <https://doi.org/10.1002/adma.202003846>.
 - [36] L. Wu, L. Yu, Q. Zhu, B. McElhenny, F. Zhang, C. Wu, X. Xing, J. Bao, S. Chen, Z. Ren, Boron-modified cobalt iron layered double hydroxides for high efficiency seawater oxidation, *Nano Energy* 83 (2021), 105838, <https://doi.org/10.1016/j.nanoen.2021.105838>.
 - [37] D.W. Wang, Q. Li, C. Han, Q.Q. Lu, Z.C. Xing, X.R. Yang, Atomic and electronic modulation of self-supported nickel-vanadium layered double hydroxide to accelerate water splitting kinetics, *Nat. Commun.* 10 (2019) 3899, <https://doi.org/10.1038/s41467-019-11765-x>.
 - [38] G.X. Wang, W. Chen, G.L. Chen, J. Huang, C.S. Song, D.L. Chen, Y. Du, C.R. Li, K. K. Ostrikov, Trimetallic Mo-Ni-Co selenides nanorod electrocatalysts for highly-efficient and ultra-stable hydrogen evolution, *Nano Energy* 71 (2020), 104637, <https://doi.org/10.1016/j.nanoen.2020.104637>.
 - [39] Y.X. Lu, C.L. Dong, Y.C. Huang, Y.Q. Zou, Z.J. Liu, Y.B. Liu, Y.Y. Li, N.H. He, J. Q. Shi, S.Y. Wang, Identifying the geometric site dependence of spinel oxides for the electrooxidation of 5-hydroxymethylfurfural, *Angew. Chem. Int. Ed.* 59 (2020) 19215–19221, <https://doi.org/10.1002/anie.202007767>.
 - [40] H. Ebel, N. Zagler, R. Svagera, M. Ebel, R. Kaitna, Quantitative surface-analysis by total electron yield, *Fresen. J. Anal. Chem.* 353 (1995) 348–350, <https://doi.org/10.1007/bf00322066>.
 - [41] Y.T. Luo, Z.Y. Zhang, F.N. Yang, J. Li, Z.B. Liu, W.C. Ren, S. Zhang, B.L. Liu, Stabilized hydroxide-mediated nickel-based electrocatalysts for high-current-density hydrogen evolution in alkaline media, *Energy Environ. Sci.* 14 (2021) 4610–4619, <https://doi.org/10.1039/d1ee01487k>.
 - [42] H.B. Yang, S.-F. Hung, S. Liu, K. Yuan, S. Miao, L. Zhang, X. Huang, H.-Y. Wang, W. Cai, R. Chen, J. Gao, X. Yang, W. Chen, Y. Huang, H.M. Chen, C.M. Li, T. Zhang, B. Liu, Atomically dispersed Ni(I) as the active site for electrochemical CO₂ reduction, *Nat. Energy* 3 (2018) 140–147, <https://doi.org/10.1038/s41560-017-0078-8>.
 - [43] J. Jiang, F. Sun, S. Zhou, W. Hu, H. Zhang, J. Dong, Z. Jiang, J. Zhao, J. Li, W. Yan, M. Wang, Atomic-level insight into super-efficient electrocatalytic oxygen evolution on iron and vanadium co-doped nickel (oxy)hydroxide, *Nat. Commun.* 9 (2018) 2885, <https://doi.org/10.1038/s41467-018-05341-y>.
 - [44] L. Zeng, Z. Liu, K. Sun, Y. Chen, J. Zhao, Y. Chen, Y. Pan, Y. Lu, Y. Liu, C. Liu, Multiple modulations of pyrite nickel sulfides via metal heteroatom doping engineering for boosting alkaline and neutral hydrogen evolution, *J. Mater. Chem. A* 7 (2019) 25628–25640, <https://doi.org/10.1039/c9ta08030a>.
 - [45] Z. Xia, H. Zhang, K. Shen, Y. Qu, Z. Jiang, Wavelet analysis of extended X-ray absorption fine structure data: theory, application, *Phys. B Condens. Matter* 542 (2018) 12–19, <https://doi.org/10.1016/j.physb.2018.04.039>.
 - [46] A.A. Dubale, Y. Zheng, H. Wang, R. Huebner, Y. Li, J. Yang, J. Zhang, N.K. Sethi, L. He, Z. Zheng, W. Liu, High-performance bismuth-doped nickel aerogel electrocatalyst for the methanol oxidation reaction, *Angew. Chem. Int. Ed.* 59 (2020) 13891–13899, <https://doi.org/10.1002/anie.202004314>.
 - [47] Y. Chen, S. Ji, Y. Wang, J. Dong, W. Chen, Z. Li, R. Shen, L. Zheng, Z. Zhuang, D. Wang, Y. Li, Isolated single iron atoms anchored on n-doped porous carbon as an

- efficient electrocatalyst for the oxygen reduction reaction, *Angew. Chem. Int. Ed.* 56 (2017) 6937–6941, <https://doi.org/10.1002/anie.201702473>.
- [48] V. Stamenkovic, B.S. Mun, K.J.J. Mayrhofer, P.N. Ross, N.M. Markovic, J. Rossmeisl, J. Greeley, J.K. Nørskov, Changing the activity of electrocatalysts for oxygen reduction by tuning the surface electronic structure, *Angew. Chem. Int. Ed.* 45 (2006) 2897–2901, <https://doi.org/10.1002/anie.200504386>.
- [49] B. Hammer, J.K. Nørskov, Theoretical surface science and catalysis—calculations and concepts. *Advances in Catalysis: Impact of Surface Science on Catalysis*, Academic Press, 2000, pp. 71–129.
- [50] P. Sabatier, *La Catalyse en Chimie Organique*, La Catalyse en Chimie Organique, Librairie Polytechnique, Paris et Liège, 1920.
- [51] H. Ooka, J. Huang, K.S. Exner, The Sabatier principle in electrocatalysis: basics, limitations, and extensions, *Front. Energy Res.* 9 (2021), 654460, <https://doi.org/10.3389/fenrg.2021.654460>.
- [52] Y. Fu, H.-Y. Yu, C. Jiang, T.-H. Zhang, R. Zhan, X. Li, J.-F. Li, J.-H. Tian, R. Yang, NiCo alloy nanoparticles decorated on n-doped carbon nanofibers as highly active and durable oxygen electrocatalyst, *Adv. Funct. Mater.* 28 (2018), 1705094, <https://doi.org/10.1002/adfm.201705094>.
- [53] M. Liu, Y. Jiao, S. Zhan, H. Wang, Ni₃S₂ nanowires supported on Ni foam as efficient bifunctional electrocatalyst for urea-assisted electrolytic hydrogen production, *Catal. Today* 355 (2020) 596–601, <https://doi.org/10.1016/j.cattod.2019.05.032>.
- [54] R. Subbaraman, D. Tripkovic, D. Strmcnik, K.-C. Chang, M. Uchimura, A. P. Paulikas, V. Stamenkovic, N.M. Markovic, Enhancing hydrogen evolution activity in water splitting by tailoring Li⁺-Ni(OH)₂-Pt interfaces, *Science* 334 (2011) 1256–1260, <https://doi.org/10.1126/science.1211934>.